Near-Field Analysis and Design of Inductively-Coupled Wireless Power Transfer System in FEKO

Dowon Kim, Adrian T. Sutinjo, and Ahmed Abu-Siada

Department of Electrical and Computer Engineering
Curtin University, Bentley, Perth Western Australia 6102, Australia
dowon.kim@postgrad.curtin.edu.au, adrian.sutinjo@curtin.edu.au, and a.abusiada@curtin.edu.au

Abstract **─** Inductively-coupled wireless power transfer (WPT) system is broadly adopted for charging batteries of mobile devices and electric vehicles. The performance of the WPT system is sensitively dependent on the strength of electromagnetic coupling between the coils, compensating topologies, loads and airgap variation. This paper aims to present a comprehensive characteristic analysis for the design of the WPT system with a numerical simulation tool. The electromagnetic field solver FEKO is mainly used for studying high-frequency devices. However, the computational tool is also applicable for not only the analysis of the electromagnetic characteristic but also the identification of the electrical parameters in the WPT system operating in the near-field. In this paper, the self and mutual inductance of the wireless transfer windings over the various airgaps were inferred from the simulated *S*-parameter. Then, the formation of the magnetic coupling and the distribution of the magnetic fields between the coils in the series-parallel model were examined through the near-field analysis for recognizing the efficient performance of the WPT system. Lastly, it was clarified that the FEKO simulation results showed good agreement with the practical measurements. When the input voltage of 10 V was supplied into the transmitting unit of the prototype, the power of 5.31 W is delivered with the transferring efficiency of 97.79% in FEKO. The actual measurements indicated 95.68% transferring efficiency. The electrical parameters; V_{in}, V_{out}, Z_{in}, θ, I_{in}, and I_{out}, had a fair agreement with the FEKO results, and they are under 8.4% of error.

Index Terms **─** Compensation topology, FEKO, inductive power transfer, near-field analysis, magnetic coupling, wireless power transfer design.

I. INTRODUCTION

The principle of wireless power transfer (WPT) was introduced a century ago by N. Tesla [1]. He suggested that electric energy can be delivered through free space efficiently when the resonance frequency is well-tuned between the transmitting (*Tx*) and receiving (*Rx*) coil by the compensating capacitors, and modern inductively-coupled WPT systems are based on his practical model [2]. As the demands of mobile devices and electric vehicles (EVs) increase, the WPT system is broadly adopted for charging their batteries simply and safely [3-6]. WPT methods are classified into a non-radiative (also known as near-field) and radiative (also known as far-field or microwave) application. In general, the non-radiative WPT system employs the resonant coupling phenomenon between the transmitter and receiver, and it also categorized into an inductively and capacitively-coupled method [3, 7]. The capacitively-coupled WPT is used for the biomedical device and EV charging apparatus [8, 9]. However, the inductively-coupled method is widely used for the high power and the power transfer applications in the range from millimeters to a few meters [10, 11]. In this paper, WPT is used to refer to inductively-coupled WPT.

For the optimized design of the WPT device, it is essential to analyze both electromagnetic phenomena (i.e., magnetic field and coupling between the coils) and electrical components (i.e., inductance and transferred power) prior to the practical implementation. FEKO is the electromagnetic field solver [12], and it is mainly employed for analyzing radio frequency components, antennas and radiations [13-15]. The previous research presented that FEKO is employed to examine the power transfer efficiency of the near-field WPT system in different material between the antennas [16]. The application of FEKO was introduced for analyzing scattering parameter (*S*-parameter), input impedance and wire structure in the range of frequency of 10-11.5 MHz [17], however, the magnetic coupling study was not presented. In addition, the numerical value of the magnetic field between *Tx* and *Rx* of the WPT system were examined over the variation of transfer distance [18, 19]. However, it did not cover the application for the design or analysis of WPT performance, and the simulation tool was utilized for the partial inspection of WPT performance. This paper aims to introduce the comprehensive implementation process of the 20 kHz WPT system using FEKO. The various frequency ranges

Submitted On: January 30, 2019
Accepted On: December 28, 2019

such as 140 kHz, 85kHz, and 20 kHz have been adopted in different regions based on the frequency allocation [20-23]. For reducing the high-frequency loss and the emission of the electromagnetic field, this study conducted in the frequency of 20 kHz.

A WPT system is mainly composed of the high-frequency (HF) source, *Tx* and *Rx* coils, and load unit, as shown in Fig. 1. In the practical WPT device, the HF source is generated by a switching device such as a half or full-bridge inverter, and the load unit has a rectifying device to obtain DC power from the transferred HF source. For accurate analysis of the switching process in the DC/AC or AC/DC circuit, specialized simulation tools are required. However, the HF source and load unit in FEKO can be described on the wire ports, and the inductive coupling behavior in the transferring part can be simulated in the numerical simulation software. Furthermore, the self and mutual inductance of the WPT coils can be extracted from the results of the *S*-parameter, and the transferred power in different load and air-gap are predictable. Accordingly, FEKO provides precise analysis for the formation and distribution of magnetic coupling between the coils. Also, it provides the electrical parameters of the simplified WPT circuit in the wire ports, as shown in Fig. 1.

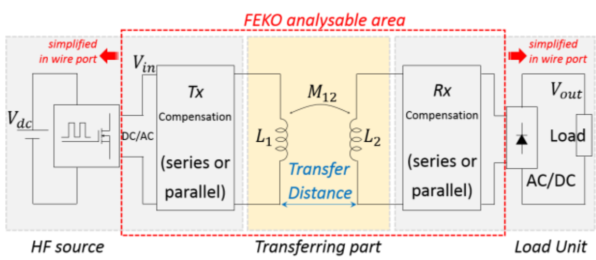

Fig. 1. Inductively-coupled WPT system.

In Section II, it is presented how the self and mutual inductance of the *Tx* and *Rx* coil are identified. Sections III and IV explain the compensating topologies for tuning the resonance frequency, then, the strength of the magnetic coupling over the various airgaps is explored at the resonance frequency of 20 kHz. Consequently, the practical measurements to examine the transferred power, output voltage and other electrical parameters of the WPT prototype are conducted, and the results are compared with the FEKO results in Section V.

II. SELF AND MUTUAL INDUCTANCE OF COILS

The traditional transformer can be described as a two-port network, as indicated in Fig. 2, and the impedance parameter (*Z*-parameter) in the network is convertible to the *S*-parameter [24]. Therefore, the self-inductance (L_1 and L_2) and mutual-inductance, M_{12}, constructed in the simulation tool can be inferred from the *S*-parameters. When the voltage source V_{in} with the resistance R_o excites the two-port networks in the *Tx*, the impedance matrix is expressed in (1), and the self and mutual impedance of coils are determined through (2) and (3):

$$\begin{bmatrix} V_{in} \\ 0 \end{bmatrix} = \begin{bmatrix} R_o + j\,\omega L_1 & j\,\omega M_{12} \\ j\,\omega M_{12} & R_L + j\,\omega L_2 \end{bmatrix} \begin{bmatrix} I_1 \\ I_2 \end{bmatrix} = \begin{bmatrix} R_o + Z_{11} & Z_{12} \\ Z_{21} & R_L + Z_{22} \end{bmatrix} \begin{bmatrix} I_1 \\ I_2 \end{bmatrix}, \tag{1}$$

$$Z_{11} = Z_{22} = \frac{(R_o + S_{11}R_o)(1-S_{22}) + S_{12}S_{21}R_o}{(1-S_{11})(1-S_{22}) - S_{12}S_{21}}, \tag{2}$$

$$Z_{12} = Z_{21} = \frac{2S_{21}(R_oR_L)^{1/2}}{(1-S_{11})(1-S_{22}) - S_{12}S_{21}}. \tag{3}$$

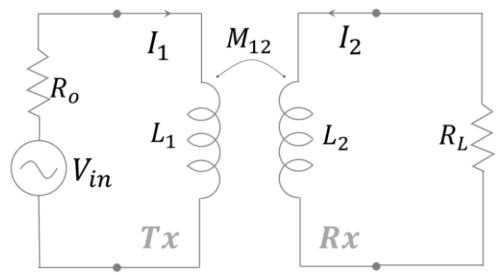

Fig. 2. Traditional transformer model.

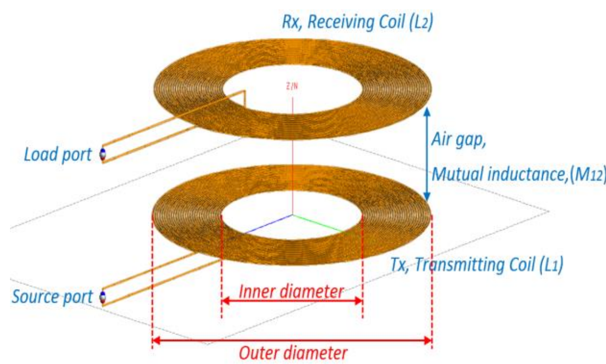

Fig. 3. WPT system model for calculating the self and mutual inductance of coils.

Table 1: Property of the practical coils

Property	Value
Inner Diameter of *Tx* and *Rx*	210 mm
Outer Diameter of *Tx* and *Rx*	400 mm
Number of Turns	30
Type of Wire	Litz-wire 1,650 filaments (0.05 mm diameter)
Radius of Wire	1.5 mm
Parasitic Resistance of Wire	5.962 Ω/km up to 850 kHz
Medium of Space	Air

The planar spiral coil was built to economize the space, as shown in Fig. 3, and the properties of the practical coil are presented in Table 1. The loss caused by the skin effect at 20 kHz was ignored in this study. However, the actual coil was built with 1,650 stranded filaments Litz-wire to secure the versatility for the higher frequency systems. Besides, the WPT system at low frequency can be free from the skin effect. However, the system needs more turns of coils to produce enough magnetic field, and the transferring distance can be decreased at the low frequency because of the low value of the quality factor. For example, the WPT system at the utility frequency of 60 Hz was introduced and The application implemented with the coil of 450 turns [25].

The simulations to obtain the *S*-parameters were conducted in the different transfer distance (10, 55, 100, 150, and 200 mm) over the frequency range from 15 kHz to 25 kHz as shown in Fig. 4. The source R_o and load resistance R_L are set 50 Ω, respectively, during the simulations. The value of self-inductance L_1 and L_2 is constant regardless of the air-gap, and the mutual-inductance M_{12} and the coupling coefficient k_{12} are correctly calculated based on (4) and (5). The coils in the simulation were constructed by the copper wire. It was also found that the inductance values present repetitively in the various frequency range,

$$L_1 = \frac{|Z_{11}|}{\omega}, L_2 = \frac{|Z_{22}|}{\omega}, \tag{4}$$

$$M_{12} = \frac{|Z_{12}|}{\omega}, k_{12} = \frac{M_{12}}{\sqrt{L_1 L_2}}. \tag{5}$$

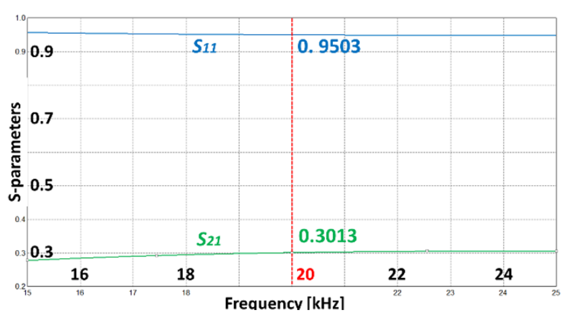

(a)

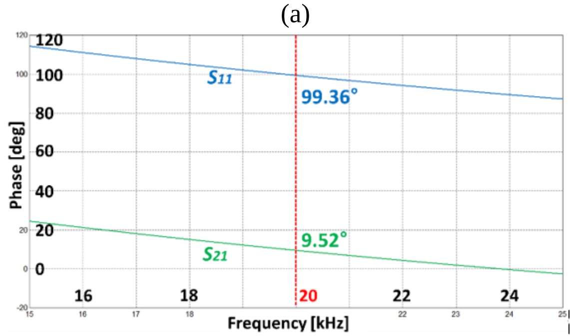

(b)

Fig. 4. Example of *S*-parameter result at 100 mm air gap: (a) absolute and (b) phase angle.

Table 2: *S*-parameter at 20 kHz

Air-Gap [mm]	S_{11} at 20 kHz		S_{21} at 20 kHz	
	Magnitude	Phase Angle	Magnitude	Phase Angle
10	0.6038	114.71°	0.7929	24.94°
55	0.8719	103.08°	0.4831	13.25°
100	0.9503	99.36°	0.3013	9.52°
150	0.9793	97.94°	0.1870	8.09°
200	0.9896	97.42°	0.1214	7.58°

This work considered the implantation of the WPT system for the charging device at the frequency of 20 kHz. Hence, the magnitude and phase angle of *S*-parameter at the frequency of 20 kHz are shown in Table 2. To verify the accuracy of the FEKO results, the actual inductance value of the built coil was measured by frequency response analyzer (FRA, DOBLE M5300). For reference, the passive electrical parameters; resistance (*R*), inductance (*L*) and capacitance (*C*), in the network can be precisely measured at the various range of frequency up to 2 MHz [26].

The results from the computational calculation in Table 3 are comparable to the experimental value, and the percentage difference of the self-inductance ($\%\Delta L_1$ and $\%\Delta L_2$) and the coupling coefficient ($\%\Delta M_{12}$ or $\%\Delta k_{12}$) is under 0.17% and 3.59%, respectively. Besides, the FEKO result indicated the resistance value of the copper coil by 0.143 Ω whereas the actual value of the parasitic resistance of L_1 and L_2 are 0.49 Ω and 0.48 Ω at 20 kHz, respectively.

III. COMPENSATION FOR RESONANCE

For tuning the resonance frequency in the *Tx* and *Rx* coil, the compensating capacitor can be implemented in mainly four topologies: series-series (*SS*), series-parallel (*SP*), parallel-series (*PS*), and parallel-parallel (*PP*) as shown in Fig. 5. As the *SS* topology as illustrated in Fig. 5 (a) is simple, and the value of the compensating capacitor C_1 at the *Tx* coil is not a function of the air gap and the load impedance, many devices use this WPT system for wireless charging applications [27-29].

However, the transfer efficiency of the *SS* topology decreases significantly when the transfer distance varies [18], and the voltage-source-type *SS* system can damage the power supply when the *Tx* does not have a coupling with the *Rx* unit [30]. Also, the transfer efficiency can be reduced significantly when the two coils are coupled at the nearer distance than the critical distance. It is defined as a frequency bifurcation [31]. To avoid this phenomenon, it might be necessary to adjust the switching frequency, value of compensating capacitance or load resistance [32]. *SP*, *PS*, and *PP* topologies are illustrated in Figs. (b), (c), and (d). They require the precise technique for tuning the resonance frequency [33].

Table 3: Comparison of inductance value between FEKO results and practical measurements

Air Gap [mm]	Parameters Extracted by FEKO			Practical Measurement and Accuracy						
	L_1, L_2 [μH]	M_{12} [μH]	k_{12}	L_1 [μH]	$\%\Delta L_1$	L_2 [μH]	$\%\Delta L_2$	M_{12} [μH]	k_{12}	$\%\ \Delta M_{12}$ or $\%\Delta k_{12}$
10	351.7	308.5	0.877	352.2	-0.14%	351.1	0.17%	311.4	0.885	-0.91%
55	351.7	175.0	0.498	352.2	-0.14%	351.1	0.17%	175.7	0.500	-0.40%
100	351.7	107.7	0.306	352.2	-0.14%	351.1	0.17%	111.6	0.317	-3.59%
150	351.7	66.6	0.189	352.2	-0.14%	351.1	0.17%	64.9	0.184	2.65%
200	351.7	43.2	0.123	352.2	-0.14%	351.1	0.17%	41.9	0.119	3.25%

The performance degradation due to the frequency bifurcation in these topologies should also be considered. For supplying a sinusoidal HF voltage into the WPT resonant circuit, additional series inductor is required for the *Tx* side in *PS* and *PP* system to filter the harmonics from the square waveform generated by the switching device [34], and the *SS* and *SP* topologies are more suitable for the high power WPT applications [35].

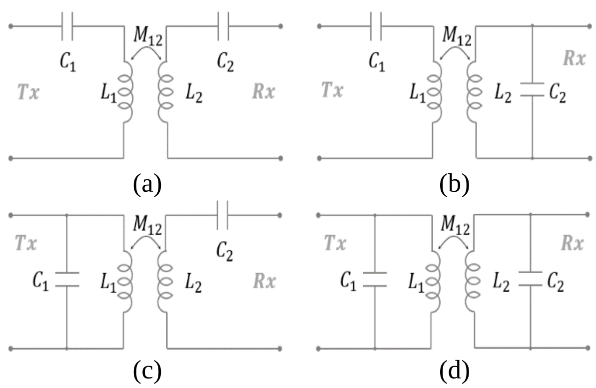

Fig. 5. Compensating topologies based on C_1 location: (a) series-series (*SS*), (b) series-parallel (*SP*), (c) parallel-series (*PS*), and (d) parallel-parallel (*PP*).

The input voltage V_{in} across the *Tx* terminals of the *SS* and *SP* topology, as shown in Figs. 5 (a) and (b) is described as in the following equations:

$$V_{in,ss} = Z_{in,ss} I_1 = \left(jX_1 + \frac{\omega^2 M_{12}^2}{R_L + r_1 + jX_2} \right) I_1 \ , \tag{6}$$

$$V_{in,sp} = Z_{in,sp} I_1 = \left(jX_1 + \frac{\omega^2 M_{12}^2}{j\,\omega L_2 + r_2 + \frac{R_L}{1 + j\,\omega C_2 R_L}} \right) I_1 \ . \tag{7}$$

Where $X_1 = \omega L_1 - (1/\omega C_1)$, $X_2 = \omega L_2 - (1/\omega C_2)$, and R_L is the load resistance. r_1 and r_2 are the parasitic resistance at *Tx* and *Rx*, respectively. As this prototype aims to achieve maximum power efficiency, it is assumed that the source impedance is zero [36, 37].

In (6) and (7), the equivalent input impedances are $\omega^2 M_{12}^2 / R_L$ and $M_{12}^2 R_L / L_2^2$, respectively, when the reactive components are eliminated by C_1 and C_2, and the parasitic resistance is ignored. If the resonance frequency is determined as follows:

$$f_o = \frac{1}{2\pi\sqrt{L_2 C_2}} \ . \tag{8}$$

The compensating capacitor C_1 in the *SS* and *SP* system, respectively, is as follows:

$$C_{2,sp} = \frac{1}{(2\pi f_o)^2 L_2} \ , \tag{9}$$

$$C_{1,sp} = \frac{1}{(2\pi f_o)^2 (L_1 - M_{12}^2 / L_2)} \ . \tag{10}$$

It is clarified that the elimination of the imaginary part of the input impedance in the *SS* topology is not affected by the variation of mutual inductance M_{12} or load resistance R_L. On the other hand, the value of the compensating capacitor $C_{1,sp}$ at the *Tx* side must be correctly selected due to the variation of M_{12} which represents the amount of the air gap between the coils.

Also, the compensating topology should be selected with the consideration of the load resistance value. If the load resistance R_L is smaller than the characteristic impedance at *Rx*, *SS* compensating system is beneficial because the input impedance $(\omega^2 M_{12}^2 / R_L)$ at the resonance frequency is inversely proportional to load resistance. It means that the WPT system can deliver much power to the input impedance, including the load resistance. The characteristic impedance Z_o is determined in (11), and Z_o of the prototype is about 44 Ω at the frequency of 20 kHz,

$$Z_o = \sqrt{L_2 / C_2} \ . \tag{11}$$

Besides, if the load resistance R_L is higher than the characteristic impedance Z_o, *SP* topology is superior to the *SS* system. Hence, *SS* and *SP* system should not be compared with the identical value of the load resistance. In this study, the near-field analysis in *SP* compensating topology is conducted in this work.

IV. MAGNETIC COUPLING AND FIELD DISTRIBUTION IN NEAR-FIELD

In the previous Sections II and III, the required electrical parameters: L_1, L_2 and M_{12}, were obtained precisely, then the value of the compensating capacitor C_1 and C_2 at the *Tx* and *Rx* side can be calculated based on (9) and (10).

When the *Tx* and *Rx* coil are loosely coupled in the magnetic field at the resonance frequency, the electric energy transfers efficiently through free space [7]. For tuning the resonance frequency of 20 kHz in the simulation models, the compensating capacitor C_2 at the *Rx* side was selected as 180 nF at the self-inductance value of 351 μH on L_2 at the frequency of 20 kHz.

The compensating capacitor C_1 for the *SP* topology should be employed from (10) with respect to the air gap as the mutual inductance M_{12} varies over the transfer distance. The value of the compensating capacitor is independent of the load resistance in the *SP* system. However, the low load resistance and near airgap can cause a frequency bifurcation and efficiency reduction [31]. The compensating capacitors at both *Tx* and *Rx* side were implemented on the wire port and the AC voltage of 10 V_{peak} at 20 kHz was supplied into the *Tx* unit during the simulation. As mentioned earlier, the process of the high-frequency switching is not assessable in FEKO, however, the peak magnitude of the voltage input V_{in} to the *Tx* unit can be extracted by the Fourier series analysis in (12):

$$V_{in} = V_{dc}\,\frac{4}{\pi}\sum_{k=1}^{\infty}\frac{\sin\{(2n-1)\omega t)}{(2n-1)}\ [\mathrm{V}]\,. \tag{12}$$

The input voltage V_{in} is generated in the shape of a square waveform by the DC to AC inverter across the terminal of the *Tx* coil. Hence, the sinusoidal waveform of the input voltage; also, it represents the first harmonic of the square waveform, where V_{dc} is the magnitude of the square waveform, and n is the number of harmonics. In the experiments, the square wave voltage of 7.9 V is to be injected into the *Tx* unit, the AC voltage of 10 V is applied for the FEKO simulation based on (12).

Furthermore, the equivalent load resistance R_{eq} can be determined through (13) when the full-bridge rectifier is utilized between the *Rx* unit and the road resistance R_L [38],

$$R_{eq} = \frac{8}{\pi^2}R_L\ [\Omega]. \tag{13}$$

In the FEKO analysis, the equivalent resistance R_{eq} was set as 97 Ω at the AC output terminals of *Rx* unit. It states that the actual load resistance across the DC output terminal is about 120 Ω. The induced magnetic field in the *Rx* coil by *Tx* coil, strength and distribution of the magnetic field are illustrated in Fig. 7. The simulation results confirm that the efficiency of the WPT system declines when the air gap is over the limit of magnetic coupling range discovered by the simulation result. For reference, this electromagnetic analysis of FEKO was conducted by the student edition.

The level of the magnetic field at both *Tx* and *Rx* coil indicates about 40 A/m and 100 A/m at the 10 mm and 55 mm air gap, respectively as shown in Figs. 7 (a) and (b). At the distance of 100 mm, the amplitude of magnetic field in the *Tx* coil is higher than in the *Rx* coil, but *Rx* coil has the similar amount of the magnetic field in *Tx* coil as shown in Fig. 7 (c). The highest level of the 500 A/m magnetic field is recorded at the 150 mm airgap though the *Rx* coil has the induced magnetic field of 250 A/m as shown in Fig. 7 (d).

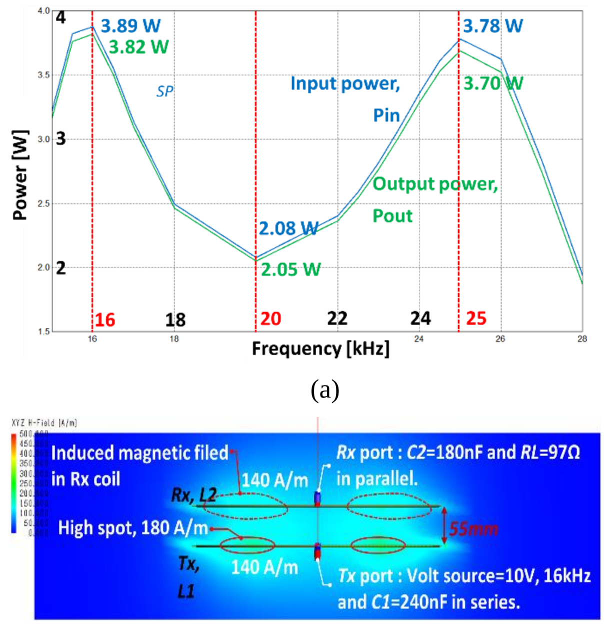

(a)

(b)

Fig. 6. Transferring power and magnetic field distribution in *SP* topology at 55 mm: (a) Supplied power and transferred power across the load, and (b) magnetic coupling at the frequency of 16 kHz.

It is verified that the low magnetic field is formed between the *Tx* and *Rx* coil at the near gap at the frequency of 20 kHz; hence, low power is delivered from the *Tx* unit to the *Rx* unit. It is caused by the phenomena of frequency bifurcation, which occurs when two coils are coupled in the over-coupled region. The FEKO simulation can also clarify the frequency bifurcation. For instance, at the distance of 55 mm, the transferring power is only 2.05 W at 20 kHz, however, at the frequency of 16 kHz and 25 kHz, the power of 3.82 W and 3.70 W is delivered to the Rx unit, respectively as illustrated in Fig 6 (a). Also, the higher magnetic field of 140 A/m at the frequency of 16 kHz than at 20 kHz frequency is formed as shown in Fig. 6 (b) and Fig. 7 (b). To achieve the improved performance of the WPT system at the near distance, it is required to shift the switching frequency or utilize the different value of the compensating capacitor for avoiding the frequency bifurcation.

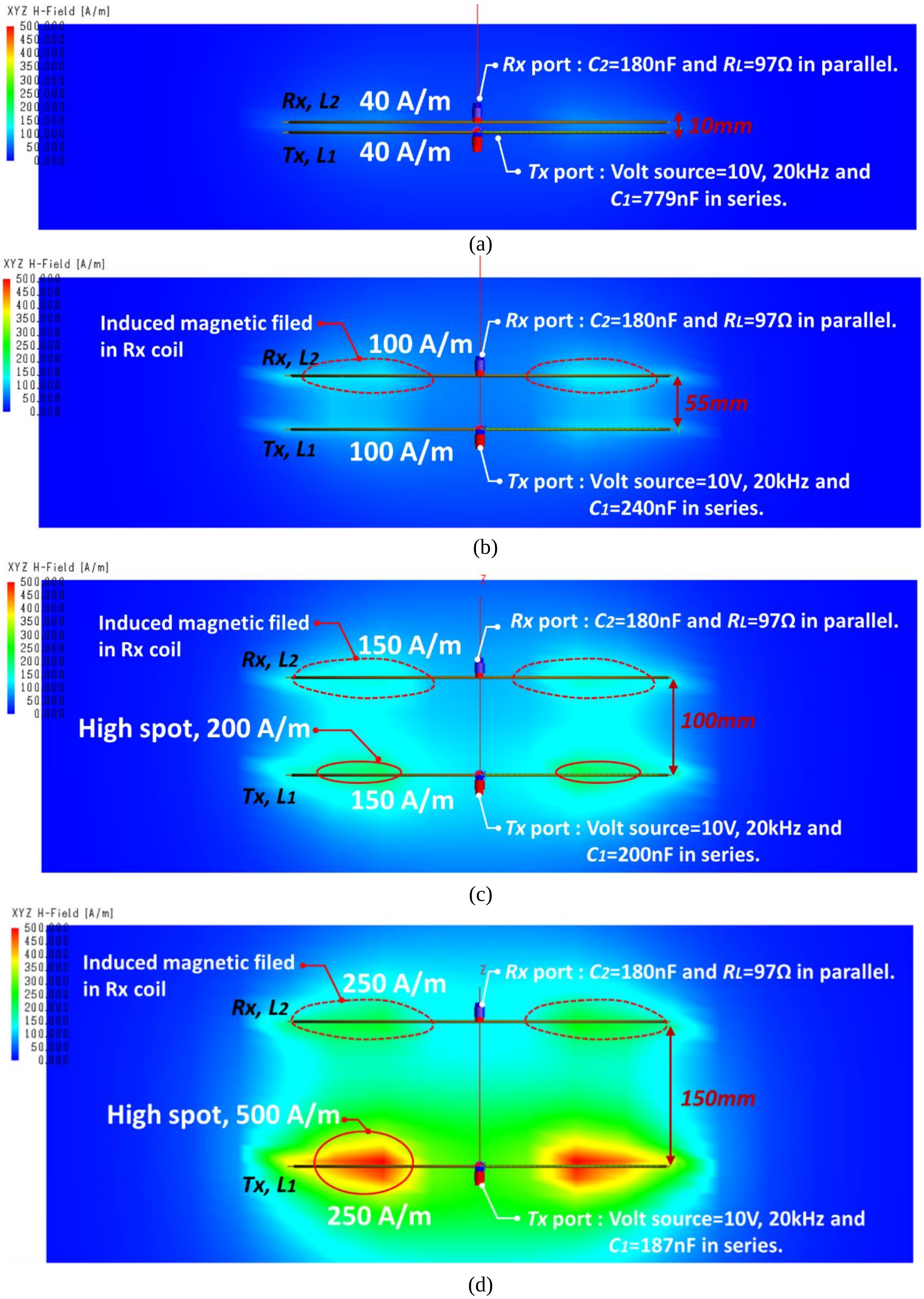

Fig. 7. Magnetic coupling and field distribution in *SP* topology over the different airgap (C_2 =180 nF) at 20 kHz: (a) 10 mm, C_1 =779 nF, (b) 55mm, C_1 =240 nF, (c) 100 mm, C_1 =200 nF, and (d) 150 mm, C_1 =187 nF.

V. POWER TRANSFERRED AND PRACTICAL VERIFICATION

For the verification of the simulation results, the transferred power and the related parameters were measured in the *SP* model at the air gap of 100 mm, as shown in Fig. 8 (a). The WPT model at the distance of 100 mm was selected as the magnetic coupling between the coils is well maintained, and the frequency bifurcation is not found at the distance. The full-bridge with gate driver (PWD 13F60, STMicroelectronics) was implemented, and the gate signals with the duty cycle of 50% at the 20 kHz frequency were given to the switching device from the micro-controller (Analog discovery 2, Digilent), as shown in Fig. 8 (b).

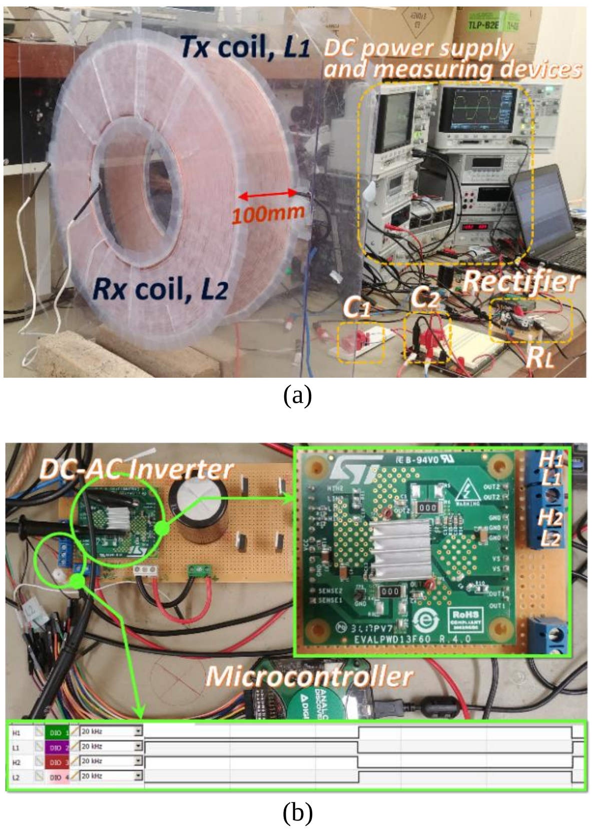

Fig. 8. Experimental measurement set-up: (a) *Tx* and *Rx* coils with compensating capacitors, and (b) full-bridge switching device and pulse (gate) signals.

In the practical experiment, the low voltage of 10 V_{peak} was supplied into the circuit due to the considerations of high voltage resonance oscillation and electromagnetic interference. As a DC power supply and HF switching devices could not be configured in the simulation tool, the overall efficiency η_o between the DC power supply and the load resistance was not evaluated. However, the transferring efficiency η_T from the *Tx* unit to the load resistance was correctly identified.

The distribution of the electric and magnetic field between two coils with the wire ports in the *SP* system at 100 mm air gap is illustrated, and it represents that the electric and magnetic fields at the middle of the coil are about 400 V/m and 200 A/m, respectively. At the vicinity of the coils, the values are under 200 V/m and 70 A/m, respectively, as shown in Figs. 9 (a) and (b). Therefore, the level of the electromagnetic field can be estimated for the safety clarification in the near-field area based on the guidelines; IEEE C95.1-2014 or International Commission on Non-Ionizing Radiation Protection [39].

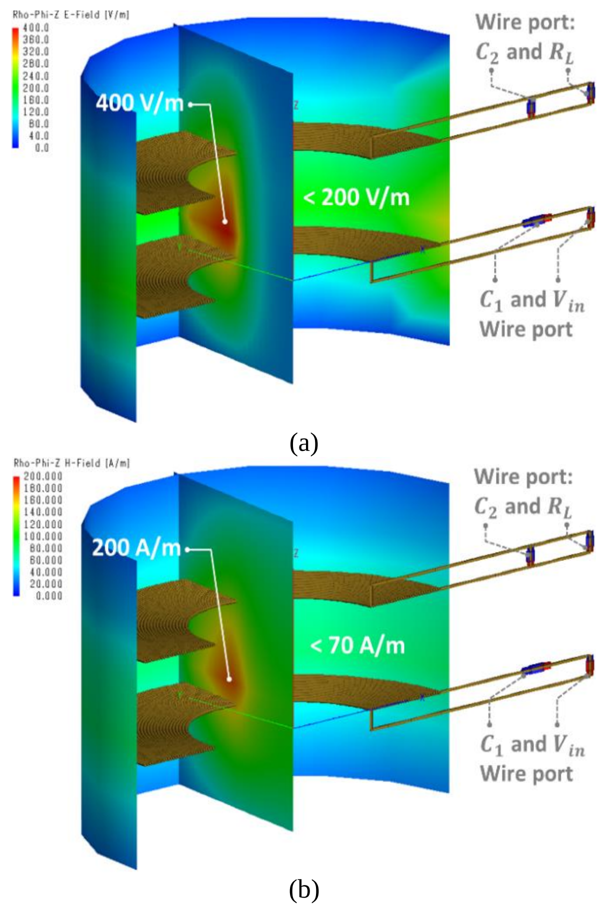

Fig. 9. FEKO results of the near-field in the *SP* system at 100 mm air gap at the frequency of 20 kHz: (a) electric field and (b) magnetic field.

The electrical parameters in the WPT model; V_{in}, V_{out}, Z_{in}, θ, I_{in}, I_{out}, P_{in}, and P_{out}, can also be determined in the different frequency range, as shown in Fig. 10. When the peak voltage of 10 V is supplied into the *Tx* unit, the output voltage of 32.1 V is produced across of the load terminal at the frequency of 20 kHz, and the input and output peak current is recorded as 1.170 A and 0.331 A, respectively, in peak value as shown in Figs. 10 (a) and (b).

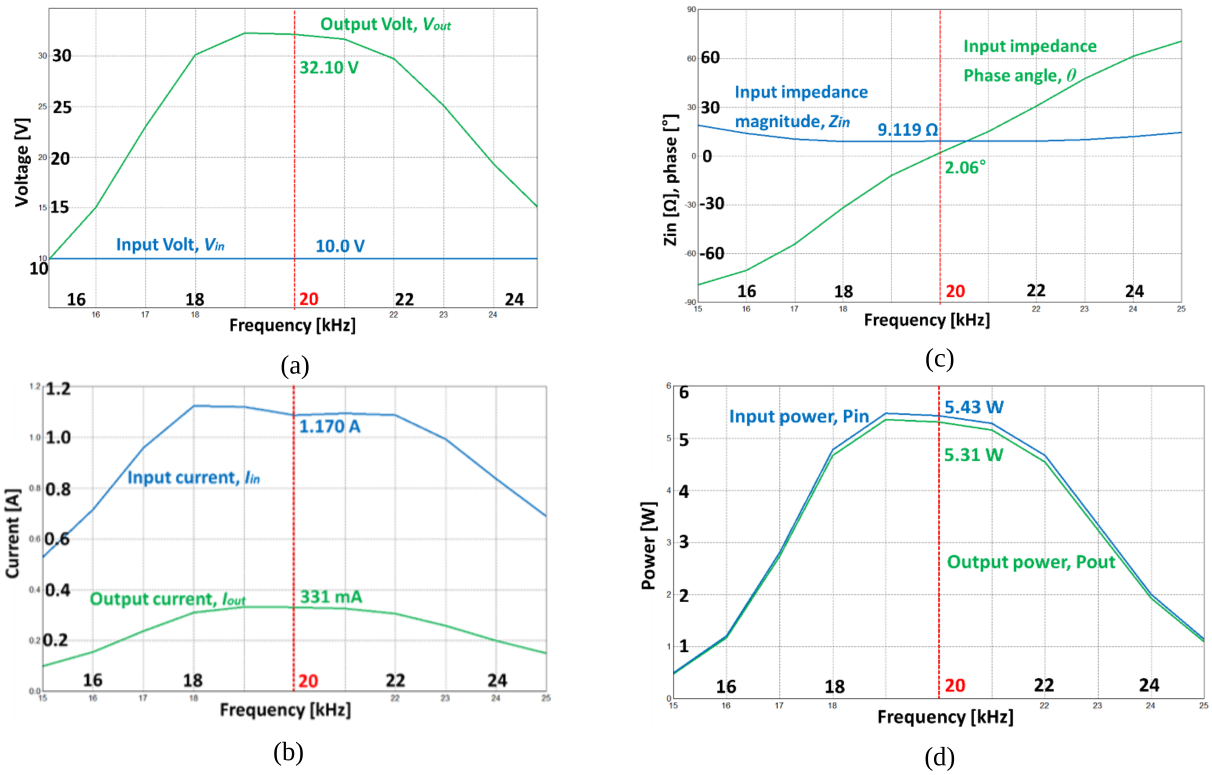

Fig. 10. FEKO results of electrical parameters of *SP* WPT system at 100 mm: (a) in/output voltage, (b) in/output current, (c) input impedance, and (d) in/output power.

Table 4: Comparison of the FEKO results and the experiment measurement in the *SP* WPT model at the 100 mm airgap

Parameters	**FEKO**	**Experimental Measurement**	**Δ Difference**	**%Δ**
V_{dc} (DC voltage)	n/a	8.7 V	n/a	n/a
I_{dc} (DC current)	n/a	0.72 A	n/a	n/a
P_{dc_in} (DC power)	n/a	6.264 W	n/a	n/a
P_{in} (Input AC Power)	5.43 W	5.897 W	-0.467 W	-8.600%
V_{in} (Input AC voltage)	n/a 10.00 V_{peak} 7.071 V_{RMS}	7.900 V_{peak} [square wave] 10.06 V_{peak} [1^{st} harmonic] 7.113 V_{RMS}	n/a n/a -0.042 V_{RMS}	n/a n/a -0.594%
I_{in} (AC in *Tx*)	1.170 A_{peak} 0.827 A_{RMS}	n/a 0.829 A_{RMS}	n/a -0.002 A_{RMS}	n/a -0.242%
Z_{in} (Input impedance)	9.119 Ω	8.580 Ω	0.539 Ω	5.911%
Θ (Phase angle of Z_{in})	2.06°	3.54°	-1.480°	n/a
V_{out} (Voltage across load)	32.10 V_{peak} 22.698 V_{RMS}	n/a 22.543 V_{RMS}	n/a 0.155 V_{RMS}	n/a 0.683%
I_{out} (Current through load)	0.331 A_{peak} 0.234 A_{RMS}	n/a 0.250 A_{RMS} [Calculated]	n/a -0.016 A_{RMS}	-6.834%
P_{out} (Output power on *Rx*)	5.31 W	5.642 W	-0.332 W	-6.252%
η_T (Transfer efficiency)	97.790%	95.676%	2.114%	2.162%
P_{dc_out} (Output power on DC Load)	n/a	4.752 W	n/a	n/a
η_o (DC to DC, Overall efficiency)	n/a	75.862%	n/a	n/a

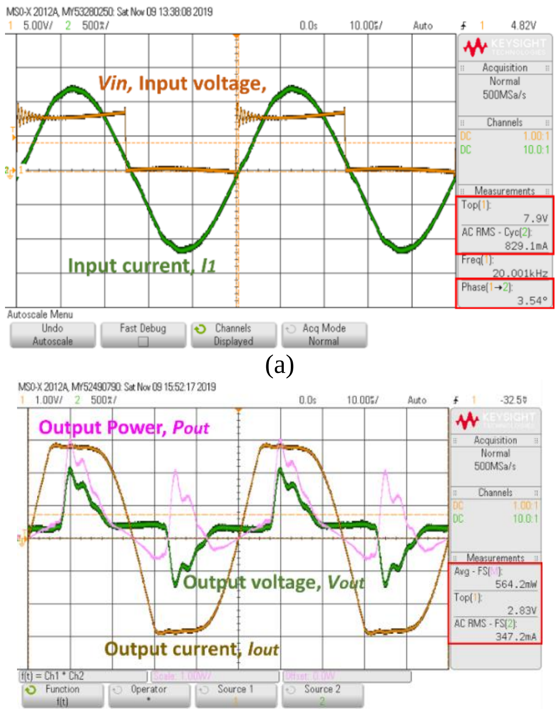

Fig. 11. Practical measurement of *SP* system at 55 mm air gap: (a) Input power and (b) output power.

The source resistance Ro was set as 0 Ω, and the load resistance of 97 Ω was implemented in the wire ports in FEKO analysis. As the compensating capacitors C_1 and C_2 were correctly utilized, the phase angle of the input impedance $Z_{in,sp}$ in (7) was 2.06°; it presents almost zero degrees, as indicated in Fig. 10 (c).

Furthermore, the transferred power between the coils was calculated and, the maximum value of the 5.31 W power was delivered at the 20 kHz frequency, as presented in Fig. 10 (d). The actual values of the parameters: V_{in}, I_{in}, V_{out}, I_{out}, and the phase angle in the prototype were measured by the oscilloscope (Agilent Technologies: MSO-X 2012A) and the current probe: Tektronix A622) as shown in Fig. 11. The results of the comparison between the simulation result and practical measurements of the WPT model are presented in Table 4. Besides, the input impedance Z_{in} of the experimental measurement in Table 4 was calculated based on the voltage and current reading on the oscilloscope.

It was observed that the percentage error of the input parameters (input voltage V_{in}, current I_{in} and impedance Z_{in}) is under 6%. The deviation value in the phase angle θ of the input impedance Z_{in}, is only 1.48°. The input and output power (P_{in} and P_{out}) in the practical measurement indicates the percentage error of -8.60% and -6.252%, respectively. The value of transfer efficiency η_T is recorded as 95.676%, and it is comparable to the FEKO result of 97.790%.

This practical measurement was conducted with the implementation of DC to HF AC inverter on the *Tx* unit and HF AC to DC rectifier. Therefore, the square waveform was indicated at the *Tx* unit, and the distorted waveforms of output voltage and current were recorded at the across of the load resistance due to the full-bridge rectifier. It is clarified that the zero-phase switching in the HF inverter was achieved as the phase difference between the voltage and current at both ends is almost zero, as shown in Figs. 11 (a) and (b).

For reference, the overall efficiency or DC to DC efficiency η_T of 75.862% is presented in the prototype due to the heat loss on the switching devices, the full-bridge rectifier, the ohmic loss in the cooper winding, etc. Consequently, the computational electromagnetic field analysis provides acceptable results for the design of the WPT systems. The formation and distribution of electromagnetic coupling between the coils, self and mutual inductance, output voltage, the rate of transferred power can be identified prior to the practical WPT implementations.

VI. CONCLUSION

The performance of the inductively-coupled WPT system is sensitive to the structure of the *Tx* and *Rx* coil, and the variation of the air gap. In this work, the characteristic of the electromagnetic field and the electrical parameters of the WPT system were correctly identified through the computational analysis and practical experiment. To demonstrate the WPT system, the *Tx* and *Rx* coil in the radius of 200 mm were implemented, and the *S*-parameter results accurately extracted the self and mutual inductance of the coils. Then, the characteristic of magnetic coupling between the two coils in the *SP* compensating WPT system at the resonance frequency of 20 kHz was observed by the near-field analysis. Also, it was found that the prototype of the *SP* system efficiently delivers electric energy when the air gap is under 100 mm. The electrical parameters (i.e., V_{in}, I_{in}, P_{in}, Z_{in}, V_{out}, I_{out}, and P_{out}) of the WPT system examined by the simulation tool are comparable to the experimental measurements of the prototype. Therefore, this study clarified that the use of FEKO facilitates the comprehensive and accurate analysis of the electromagnetic and electrical behavior of near-field WPT system.

ACKNOWLEDGMENT

This work was supported in part by the Australian Government Research Training Program and in part by the Curtin Postgraduate.

REFERENCES

[1] A. S. Marincic, "Nikola Tesla and the wireless transmission of energy," *IEEE Transactions on Power Apparatus and Systems*, vol. PAS-101, no.

10, pp. 4064-4068, doi:10.1109/TPAS.1982.317084, 1982.

[2] S. Y. R. Hui, "Past, present and future trends of non-radiative wireless power transfer," *CPSS Transactions on Power Electronics and Applications*, vol. 1, no. 1, pp. 83-91, doi: 10.24295/CPSSTPEA.2016.00008, 2016.

[3] G. A. Covic and J. T. Boys, "Modern trends in inductive power transfer for transportation applications," *IEEE Journal of Emerging and Selected Topics in Power Electronics*, vol. 1, no. 1, pp. 28-41, doi: 10.1109/ JESTPE. 2013. 2264473, 2013.

[4] A. Bindra, "Wireless power transfer is fueling the electric vehicles market [from the editor]," *IEEE Power Electronics Magazine*, vol. 4, no. 2, pp. 4-8, doi: 10.1109/MPEL.2017.2692382, 2017.

[5] Wireless EV Charging Market Worth 7,094.8 Million USD by 2025, *India Automobile News*, Available: http:// www . marketsandmarkets .com/ Market - Reports / wireless-ev-charging-market-170963517. html, Sept. 2017.

[6] X. Lu, D. Niyato, P. Wang, and D. I. Kim, "Wireless charger networking for mobile devices: fundamentals, standards, and applications," *IEEE Wireless Communications*, vol. 22, no. 2, pp. 126-135, doi: 10.1109/MWC.2015.7096295, 2015.

[7] S. Y. R. Hui, "Magnetic resonance for wireless power transfer [A look back]," *IEEE Power Electronics Magazine*, vol. 3, no. 1, pp. 14-31, doi: 10.1109/MPEL.2015.2510441, 2016.

[8] J. Dai and D. C. Ludois, "Capacitive power transfer through a conformal bumper for electric vehicle charging," *IEEE Journal of Emerging and Selected Topics in Power Electronics*, vol. 4, no. 3, pp. 1015-1025, doi:10.1109/JESTPE.2015.2505622, 2016.

[9] K. V. T. Piipponen, R. Sepponen, and P. Eskelinen, "A biosignal instrumentation system using capacitive coupling for power and signal isolation," *IEEE Transactions on Biomedical Engineering*, vol. 54, no. 10, pp. 1822-1828, doi:10.1109/TBME. 2007.894830, 2007.

[10] J. C. Lin, "Wireless power transfer for mobile applications, and health effects [Telecommun-ications health and safety]," *IEEE Antennas and Propagation Magazine*, vol. 55, no. 2, pp. 250-253, doi: 10.1109/MAP.2013.6529362, 2013.

[11] C. Park, S. Lee, G. H. Cho, and C. T. Rim, "Innovative 5-m-off-distance inductive power transfer systems with optimally shaped dipole coils," *IEEE Transactions on Power Electronics*, vol. 30, no. 2, pp. 817-827, doi:10.1109/TPEL.2014. 2310232, 2015.

[12] *FEKO Computational Electromagnetics Software*, [Online], Available: http://www.altairhyperworks. com/product/FEKO, 2019.

[13] U. Jakobus, M. Bingle, M. Schoeman, J. J. V. Tonder, and F. Illenseer, "Tailoring FEKO for microwave problems," *IEEE Microwave Magazine*, vol. 9, no. 6, pp. 76-85, doi:10.1109/MMM.2008. 929557, 2008.

[14] S. Clarke and U. Jakobus, "Dielectric material modeling in the MoM-based code FEKO," *IEEE Antennas and Propagation Magazine*, vol. 47, no. 5, pp. 140-147, doi:10.1109/MAP.2005.1599186, 2005.

[15] S. Chai, L. Guo, K. Li, and L. Li, "Combining CS with FEKO for fast target characteristic acquisition," *IEEE Transactions on Antennas and Propagation*, vol. 66, no. 5, pp. 2494-2504, doi: 10.1109/TAP.2018.2816599, 2018.

[16] I. Yoon and H. Ling, "Investigation of near-field wireless power transfer in the presence of lossy dielectric materials," *IEEE Transactions on Antennas and Propagation*, vol. 61, no. 1, pp. 482-488, doi:10.1109/TAP.2012.2215296, 2013.

[17] J. Moshfegh, M. Shahabadi, and J. Rashed-Mohassel, "Conditions of maximum efficiency for wireless power transfer between two helical wires," *IET Microwaves, Antennas & Propagation*, vol. 5, no. 5, pp. 545-550, doi:10.1049/iet-map. 2010.0134, 2011.

[18] D. Kim, A. Abu-Siada, and A. Sutinjo, "State-of-the-art literature review of WPT: Current limitations and solutions on IPT," *Electric Power Systems Research*, vol. 154, pp. 493-502, doi: https://doi.org/10.1016/j.epsr.2017.09.018, 2018.

[19] D. Kim, A. Abu-Siada, and A. Sutinjo, "A novel application of frequency response analysis for wireless power transfer system," in *2017 Australasian Universities Power Engineering Conference (AUPEC)*, pp. 1-6, doi:10.1109/AUPEC. 2017.8282474, Nov. 19-22, 2017.

[20] S. Park, "Evaluation of electromagnetic exposure during 85 kHz wireless power transfer for electric vehicles," *IEEE Transactions on Magnetics*, vol. PP, no. 99, pp. 1-1, doi:10.1109/TMAG.2017. 2748498, 2017.

[21] C. Zheng, *et al.*, "High-efficiency contactless power transfer system for electric vehicle battery charging application," *IEEE Journal of Emerging and Selected Topics in Power Electronics*, vol. 3, no. 1, pp. 65-74, doi:10.1109/JESTPE.2014. 2339279, 2015.

[22] P. Machura and Q. Li, "A critical review on wireless charging for electric vehicles," *Renewable and Sustainable Energy Reviews*, vol. 104, pp. 209-234, doi:https://doi.org/10.1016/j.rser.2019.01.027, Apr. 2019.

[23] *IEC 61980-1:2015 Electric Vehicle Wireless Power Transfer (WPT) Systems*, 2015.

[24] D. A. Frickey, "Conversions between S, Z, Y, H, ABCD, and T parameters which are valid for complex source and load impedances," *IEEE Transactions on Microwave Theory and Techniques*, vol. 42, no. 2, pp. 205-211, doi:10.1109/22.275248, 1994.

[25] H. Ishida and H. Furukawa, "Wireless power transmission through concrete using circuits resonating at utility frequency of 60 Hz," *IEEE Transactions on Power Electronics*, vol. 30, no. 3, pp. 1220-1229, doi:10.1109/TPEL.2014.2322876, 2015.

[26] D. Kim, A. Abu-Siada, and A. T. Sutinjo, "Application of FRA to improve the design and maintenance of wireless power transfer systems," *IEEE Transactions on Instrumentation and Measurement*, pp. 1-13, doi:10.1109/TIM.2018.2889360, 2019.

[27] G. Guidi, J. A. Suul, F. Jenset, and I. Sorfonn, "Wireless charging for ships: High-power inductive charging for battery electric and plug-in hybrid vessels," *IEEE Electrification Magazine*, vol. 5, no. 3, pp. 22-32, doi:10.1109/MELE.2017.2718829, 2017.

[28] Z. Li, C. Zhu, J. Jiang, K. Song, and G. Wei, "A 3-kW wireless power transfer system for sightseeing car supercapacitor charge," *IEEE Transactions on Power Electronics*, vol. 32, no. 5, pp. 3301-3316, doi:10.1109/TPEL.2016.2584701, 2017.

[29] J. H. Kim, *et al.*, "Development of 1-MW inductive power transfer system for a high-speed train," *IEEE Transactions on Industrial Electronics*, vol. 62, no. 10, pp. 6242-6250, doi:10.1109/TIE.2015.2417122, 2015.

[30] Y. H. Sohn, B. H. Choi, E. S. Lee, G. C. Lim, G. H. Cho, and C. T. Rim, "General unified analyses of two-capacitor inductive power transfer systems: Equivalence of current-source SS and SP compensations," *IEEE Transactions on Power Electronics*, vol. 30, no. 11, pp. 6030-6045, doi:10.1109/TPEL.2015.2409734, 2015.

[31] W. Chwei-Sen, G. A. Covic, and O. H. Stielau, "Power transfer capability and bifurcation phenomena of loosely coupled inductive power transfer systems," *IEEE Transactions on Industrial Electronics*, vol. 51, no. 1, pp. 148-157, doi:10.1109/TIE.2003.822038, 2004.

[32] M. Kim, J. W. Lee, and B. Lee, "Practical bifurcation criteria considering inductive power pad losses in wireless power transfer systems," *J. Electr. Eng. Technol.*, vol. 12, no. 1, pp. 173-181, doi:10.5370/JEET.2017.12.1.173, 2017.

[33] C. Jiang, K. Chau, C. Liu, and C. Lee, "An overview of resonant circuits for wireless power transfer," *Energies*, vol. 10, no. 7, p. 894, doi:10.3390/en10070894, 2017.

[34] A. J. Moradewicz and M. P. Kazmierkowski, "Contactless energy transfer system with FPGA-controlled resonant converter," *IEEE Transactions on Industrial Electronics*, vol. 57, no. 9, pp. 3181-3190, doi:10.1109/TIE.2010.2051395, 2010.

[35] Z. Bi, T. Kan, C. C. Mi, Y. Zhang, Z. Zhao, and G. A. Keoleian, "A review of wireless power transfer for electric vehicles: Prospects to enhance sustainable mobility," *Applied Energy*, vol. 179, pp. 413-425, doi:https://doi.org/10.1016/j.apenergy.2016.07.003, 2016.

[36] C. S. Kong, "A general maximum power transfer theorem," *IEEE Transactions on Education*, vol. 38, no. 3, pp. 296-298, doi:10.1109/13.406510, 1995.

[37] W. X. Zhong, C. Zhang, X. Liu, and S. Y. R. Hui, "A methodology for making a three-coil wireless power transfer system more energy efficient than a two-coil counterpart for extended transfer distance," *IEEE Transactions on Power Electronics*, vol. 30, no. 2, pp. 933-942, doi:10.1109/TPEL.2014.2312020, 2015.

[38] Z. Huang, S. C. Wong, and C. K. Tse, "Design of a single-stage inductive-power-transfer converter for efficient EV battery charging," *IEEE Transactions on Vehicular Technology*, vol. 66, no. 7, pp. 5808-5821, 2017, doi:10.1109/TVT.2016.2631596.

[39] V. Marché, "Contactless energy transfer systems finite elements modeling with flux," https://insider.altairhyperworks.com/flux-finiteelements-modeling-opitmize-contactless-energy-transfer-systems-efficiency/ (accessed), Dec. 2017.

Dowon Kim received the B.Sc. and M.Sc. degrees in Electrical Engineering from the Seoul National University of Science and Technology, Seoul, South Korea, in 2003 and 2009, respectively. He is currently pursuing the Ph.D. degree with Curtin University, Bentley, WA, Australia. From 1998 to 2011, he was a Transmission and Substation Engineer and an Engineering Lecturer with Korea Electric Power Corporation. He is a Senior Testing and Commissioning Engineer with Global Testing Services, WA, Australia since 2012. His current research interests include wireless power transfer, electromagnetics, frequency response, and power system protection.

Adrian T. Sutinjo received the B.S.E.E. degree from Iowa State University, Ames, IA, USA, in 1995, the M.S.E.E. degree from the Missouri University of Science and Technology, Rolla, MO, USA, in 1997, and the Ph.D. degree in Electrical Engineering from the University of Calgary, Calgary, AB, Canada, in 2009. From 1997 to 2004, he was an RF Engineer with Motorola, Chicago, IL, USA, and with Murandi Communications Ltd., Calgary, AB, Canada. He is currently a Senior Lecturer with the School of Electrical Engineering, Computing and Mathematics, Curtin University, Perth, WA, Australia, where he has been with the International Centre for Radio Astronomy Research since 2012. His current research interests include antennas, RF and microwave engineering, electromagnetics, and radio astronomy engineering.

Ahmed Abu-Siada received the B.Sc. and M.Sc. degrees in Electrical Engineering from Ain Shams University, Cairo, Egypt, in 1998, and the Ph.D. degree in Electrical Engineering from Curtin University, Bentley, WA, Australia, in 2004. He is currently a Discipline Lead of the Electrical and Computer Engineering, Curtin University. His current research interests include power system stability, condition monitoring, power electronics, and power quality. Abu-Siada is an Editor-in-Chief of the International Journal Electrical and Electronic Engineering, a regular reviewer for various IEEE Transactions, and a Vice-Chair of the IEEE Computation Intelligence Society, WA Chapter.